Nano-statistics: quantification and visualization of Pt cathode degradation *via* correlative electron and X-ray imaging

Authors: Liqun Kang,[1][#] Ruoyu Xu,[1][#] Jay Hon Cheung Yan,[1][#] Fernando Cacho-Nerin,[2] Julia E. Parker,[2] Christopher S. Allen,[3,4] Feng Ryan Wang[1]*

[1] Department of Chemical Engineering, University College London, Torrington Place, London, WC1E 7JE, United Kingdom.

[2] I14 Hard X-ray Nanoprobe Beamline, Diamond Light Source, Ltd., Harwell Science and Innovation Campus, Didcot, Oxfordshire OX11 0DE, United Kingdom.

[3] Electron Physical Science Imaging Centre, Diamond Light Source, Ltd., Harwell Science and Innovation Campus, Didcot, Oxfordshire OX11 0DE, United Kingdom.

[4] Department of Materials, University of Oxford, Parks Road, Oxford, OX1 3PH, United Kingdom

[#]These authors contributed equally: Liqun Kang, Ruoyu Xu, Jay Hon Cheung Yan

*Correspondence to: ryan.wang@ucl.ac.uk.

Abstract

Catalytic degradation in proton exchange membrane fuel cells (PEMFCs) has always been a challenging subject. Despite the monumental research on the subject[1-6], the complex relationship between the catalyst deactivation mechanisms and electrochemical degradation remains obscure owing to the heterogenous nature of the catalyst structure. Here we report a correlative electron and X-ray imaging method that enables a multi-modal and multi-length-scale quantification and visualisation of Pt degradation mechanisms in the oxygen reduction reaction (ORR) for proton exchange membrane fuel cell (PEMFC). This technique provides statistical information of up to 10^7 Pt nanoparticle with 2-dimensional (2D) statistical distribution of Pt content and nanoparticle number in length scales from 2 nm to 20 µm. With the accelerated durability test (ADT) under an O_2-saturated 0.1 M $HClO_4$ electrolyte between 0.4 and 1.2 V *vs.* reversible hydrogen electrode (RHE), the statistical results reveal that the carbon supported Pt nanoparticle catalyst experiences 1) 1:1.5 ratio between the type I degradation mechanisms, Pt dissolution and particle detachment, and type II, Ostwald ripening and particle agglomeration; 2) electrocatalytic activity losses of 33.4% and 41.8% for type I and II degradations, respectively; and 3) macro-scale Pt redistribution from Pt dense regions to sparse regions at an average distance of 1.6 ± 0.9 µm.

Introduction

Nanoparticles are widely studied and practically used in physical science[7], engineering[8], biology[9] and medical applications[10]. Despite the large volume of research into nanoparticles, there is little statistical analysis of them. Obtaining such statistics is valuable to understand both the collective and individual behaviours of nanoparticles in order to optimize their performance[11-13]. Here we define the concept of Nano-Statistics as quantifying both the static (e.g. element distribution, particle number, size, shape) and dynamic (e.g. growth, aggregation, leaching, movement and phase transition) properties of nanomaterials. Nano-Statistics provide a quantitative understanding of nanomaterials and help predict collective nanoparticle behaviour at application relevant scales and requires advanced imaging techniques over multiple modal and length scales. Fluorescence microscopy is a common technique employed at the micrometre scale for labelled and monitoring nanoparticles within cellular systems[14,15].

In a study by Summers *et al.*, fluorescence microscopy was utilised to examine nanoparticle delivery and dosage in cellular systems[16] and to trace cell populations[17]. Electron microscopy (EM) provides morphological and elemental information of individual nanoparticles from the nanometre scale down to atomic resolution, where changes in particle size distributions[18] and porosity[19] have been used to investigate degradation of oxygen reduction reaction (ORR) catalysts. In combination with energy dispersive spectroscopy (EDS) and identical location (IL) imaging[20-24], exposed crystal facets and elemental distribution of individual Pt based alloy nanoparticles can further be tracked at different degraded states to explain the enhanced ORR performance[25,26].

Unfortunately, current microscopy techniques still fall short in bridging towards understanding in macroscopic performance of nanomaterials. Typical electron micrographs with well-resolved nanoparticles are restricted to small field of views with particle number of questionable statistical significance[27]. Manual particle counting is also time consuming and laborious, and computational approaches are limited to thin layers or well dispersed nanoparticle systems[27-29]. Moreover, dynamically tracking nanoparticles require complex *in situ* experimental setup and analysis procedures[30,31], further impairing the understanding of the highly convoluted catalytic degradation mechanisms. Therefore, a reliable method that can overcome such limitations while utilising the unique advantages of EM is crucial to advancing the quantitative understanding of nanomaterial performance and degradation.
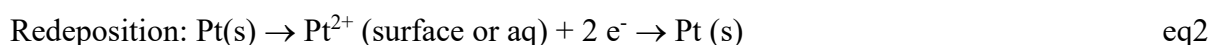
Correlative microscopy has long been adopted to connect the resolution gap to reveal multiscale structural morphologies[32,33]. This concept has recently been applied with X-ray imaging techniques. A same-view membrane cell was developed to achieve correlative EM – EDS / nano-X-ray absorption fine structure imaging on Pt based catalysts in membrane electrode assembly[34-36], revealing a correlation between S and F species from the Nafion ionomer and the presence of Pt^{2+} species in nano-cracks after electrochemical degradations[36,37]. Whilst insightful in the microscopy level, it remains uncertain how these observations translate into the macroscopic electrocatalytic degradation. Here, using a multi-modal and multi-length-scale correlative electron and X-ray imaging technique, we report the statistics of the electrocatalytic degradation mechanisms for ORR of 10^7 Pt nanoparticles. First, a 2D particle number distribution containing up to 10^7 nanoparticles at the micrometre-scale is established by correlating Pt fluorescence signals to counted nanoparticle number. Second, the Pt dissolution/particle detachment and Ostwald ripening/particle agglomeration mechanisms and the macro-scale Pt redistribution caused by corrosion of the carbon support are quantified from the macroscopic level of 10×10 μm^2 down to the microscopic level of 100×100 nm^2. These results offer a statistical understanding of the electrochemical degradations of Pt ORR catalysts by overcoming the existing disadvantages of either single microscopy technique, highlighting the importance of correlative imaging at multiple length scale.

Results and Discussion

Pt degradation, imaging and analysis protocol

Degradation mechanisms of carbon supported platinum nanoparticle (Pt/C) catalysts in PEMFCs are conventionally categorised into primary and secondary pathways based on the causality with the operating conditions[4-6]. The primary mechanisms – Pt dissolution (eq1) and carbon corrosion – are direct oxidations of the Pt catalyst and carbon support by the high operation potentials[38-40]; while the secondary mechanisms – particle agglomeration, detachment, and Ostwald ripening (eq2) – are subsidiary effects derived from the oxidised Pt^{2+} and weakened carbon support anchorage by the primary mechanisms[41-43]. However, to investigate the effects of the catalyst degradation mechanisms, an alternative categorisation

based on the apparent effects are proposed. Type I: Pt dissolution and particle detachment, where catalytic activity is loss due to an absolute reduction in the quantity of Pt catalyst from the electrode (Fig. 1a,c); Type II: Ostwald ripening and particle agglomeration, where active surface areas are reduced due to particle coarsening and decrease in particle number with the retention of Pt content (Fig. 1b,d); Type III: Carbon corrosion, apparent redistribution of Pt catalyst in the macro-scale with no direct change to the Pt nanoparticles and catalytic activity. By exploiting the commonalities in the effects of this proposed categorisation, quantifications between the different types of degradations can be achieved through the statistics of Pt content and particle number.

Leaching: $Pt(s) \rightarrow Pt^{2+} (aq) + 2 e^-$ eq1

Redeposition: $Pt(s) \rightarrow Pt^{2+} (surface\ or\ aq) + 2 e^- \rightarrow Pt (s)$ eq2

Correlative identical location transmission electron microscopy – X-ray fluorescence (IL-TEM-XRF) imaging technique is employed at progressive degradation stages of the Pt/C catalysts (Supplementary Fig. 1). High angle annular dark field scanning transmission electron microscopy (HAADF-STEM) images can measure the size, morphology, and number of Pt nanoparticles with resolution up to 0.1 – 1 nm (Supplementary Fig. 2,3). On the other hand, XRF imaging can measure significant larger areas in the order of micrometres (Supplementary Fig. 6) with spatial resolution up to 50 – 100 nm as defined by the X-ray probe size (Supplementary Figs. 4,5). XRF-nanoprobe also possesses high spectral sensitivity which provides spatially resolved quantitative information on elemental compositions of a catalyst[44,45].

Both STEM and nanoprobe XRF imaging of the Pt/C catalysts are performed on an Au TEM finder grid. By utilising the pre-patterned locator marks on the labelled grid (Supplementary Fig. 1a), the identical locations of the catalyst nanoparticles can be located at different degraded states[20-23]. Between each correlative identical location imaging session, the same catalyst-coated Au finder grid undergoes 6,000 and 10,000 cycles of accelerated durability test (ADT) between 0.4 – 1.4 V *vs.* RHE under an O_2-saturated $HClO_4$ electrolyte in a three-electrode rotating disk electrode (RDE) half-cell setup. Using this protocol, a multi-modal and multi-length-scale identical location characterisation at progressive catalyst degradation stages is performed.
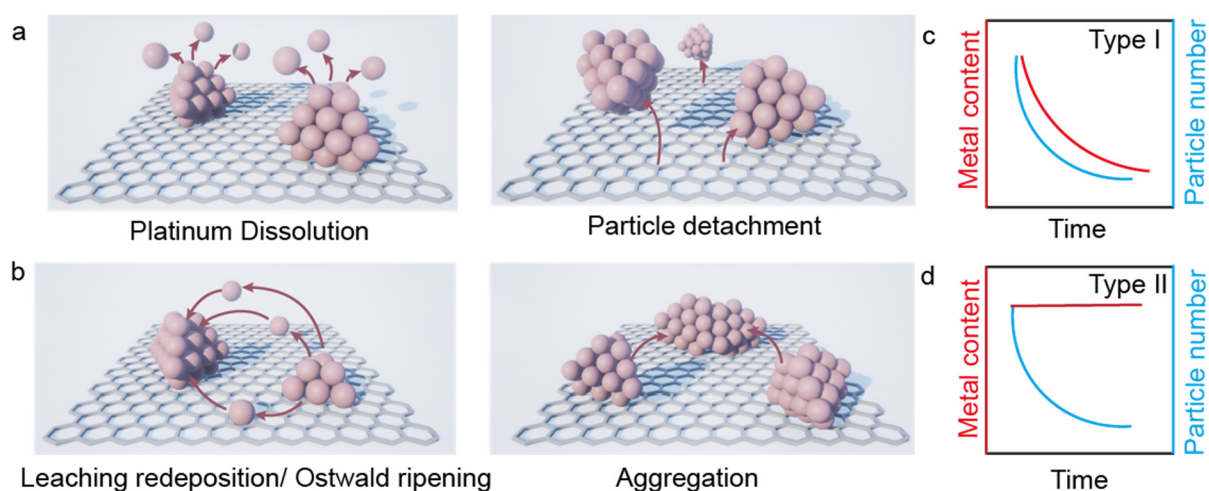

Figure 1. Chemical nature of four Pt electrochemical deactivation pathways in ORR. a, type I: Pt dissolution and particle detachment; **b,** type II: Ostwald ripening and particle

agglomeration; **c,d** Corresponding change of metal content and particle number for **a** and **b**, respectively.

2D Pt Particle Number Distribution and Quantification of Type I and II Degradation Mechanisms

A series of XRF maps is taken at 10×10 μm^2, 5×5 μm^2 and 2.5×2.5 μm^2 areas at two locations labelled L and Q on the finder grid. The Pt XRF signal of each pixel is extracted from batch peak fitting of Pt-L$_3$-M$_5$ (Lα$_1$) signal and is calibrated with Ar-K-L$_3$ (Kα$_1$) signal to account for both I$_0$ background and X-ray attenuation from the atmosphere. This normalises Pt XRF intensities across different experimental sessions to be proportional to the irradiated Pt mass and is represented as relative quantities of Pt present in the scanned area (Fig. 2a, Supplementary Fig. 8a, and methods). The integrated intensity across the entire recorded XRF map indicates the total Pt content in the image, which dropped by 36% and 61% at location L (Fig. 3a); and 31% and 57% at location Q (Supplementary Table 1) after 6,000 and 10,000 ADT cycles, respectively. This corresponds to an average of 0.0056% type I degradation per cycle between 0 and 6,000 and 0.0064% per cycle between 6,000 and 10,000 cycles.

Correlating information uniquely obtained from the IL-TEM-XRF data pairs, enables accurate estimation of nanoparticle number at the larger micro-scale areas covered by the XRF measurements. An example of the TEM-XRF data pair recorded after 6,000 ADT cycles at location L is shown in Fig. 2a,b. Ten identical locations of 300×300 nm^2 area are selected, where the particle numbers manually counted from the HAADF-STEM image are correlated against the integrated Pt/Ar XRF signal within the ten areas (Fig. 2c,d, Supplementary Fig. 9). The resulting linear relationship between Pt XRF signal and nanoparticle numbers is then applied to the XRF map, resulting in a 2D particle number distribution across the 6.8×6.8 μm^2 scanned area (Fig. 2e,f). The integrated Pt signals of the ten areas span between 3.1 and 33.3 covering 94% of the signal range, whereas the particle size distributions are similarly relatively narrow and uniform (Supplementary Fig. 10b). This suggests the obtained linear relationship is applicable for the entirety of the XRF area. To further account for uncertainty in alignment between the TEM-XRF image pair, the errors for each 300×300 nm^2 area are also determined (Supplementary Fig. 8b). Nevertheless, it is determined that $1.00 \times 10^5 \pm 1.0 \times 10^4$ Pt nanoparticles are present in this area. This correlative IL-TEM-XRF technique demonstrates efficient "particle number statistics" across an area that is several orders of magnitudes larger than what can be reasonably performed by manual analysis, and enables further quantification of the degradation pathways.
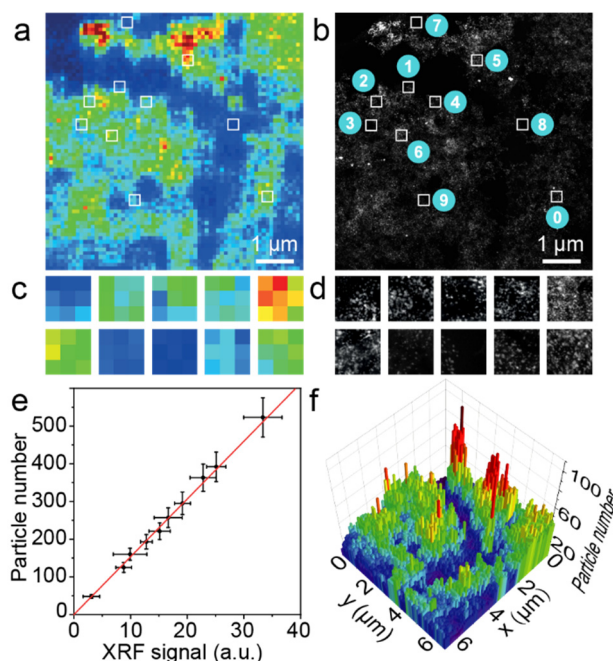
Figure 2. Correlative TEM and XRF imaging at location L after 6,000 ADT cycles. a, XRF map of Pt nanoparticles supported on conductive carbon (68 × 68 pixel, 100 nm/pixel). **b**, HAADF-STEM image at the same area of **a**. **c**, Selection of ten 3 × 3 pixel XRF maps indicated in the white box in **a**. **d**, High resolution HAADF-STEM images (300 × 300 nm^2) corresponding to the same areas shown in **c**. They are numbered and indicated in the white boxes in **b**. **e**, Plot of Pt particles numbers counted from **d** as the function of overall XRF intensity determined from **c**, forming a linear relation with r = 0.998. **f**, The map of Pt particle numbers at the 6.8 × 6.8 μm^2 area.

The same processing method is applied to all correlative TEM-XRF images at each degradation stage and location, obtaining the respective 2D particle number distributions (Supplementary Fig. 11,12). Continue with location L as an example, after 6,000 ADT cycles, the Pt nanoparticle size changes from the initial 2.8 ± 0.9 nm to a bimodal distribution with larger size of 15.9 ± 5.1 nm and smaller size of < 2 nm (Supplementary Fig. 2k,3k), while the particle number drops significantly from 1.18 × 10^5 μm^{-2} to 1.94 × 10^3 μm^{-2} and 9.82 × 10^3 μm^{-2} respectively for large and small particles (Supplementary Fig. 2k,3k). The coexistence of small and large particles suggests both type I and II degradation mechanisms take place. Assuming the quantity of Pt lost to type I mechanism can be accounted by the loss of particle number of the same proportion (Fig. 1c), it can be reasoned that 36% of the particles undergo Type I mechanism, completely lost from the catalyst either through dissolution, or detachment; 8.3% of the nanoparticles undergo dissolution only forming the smaller sized particles below 2 nm. Another 54.1% go through Type II degradation, either oxidised into Pt^{2+} before redepositing onto, or agglomerated with the remaining 1.6% of nanoparticles, increasing the particle size to the 15.9 ± 5.1 nm of the larger particles (Fig. 3c).

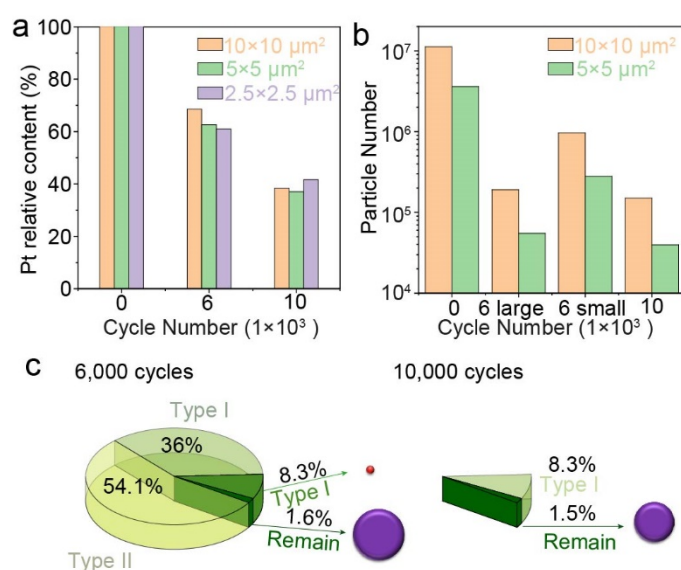**Figure 3. a**, Relative Pt content obtained from XRF maps at different ADT cycles. **b**, Absolute Pt particle numbers at different ADT cycles. **c**, Quantification of type I and II degradation mechanisms at 6,000 and 10,000 cycles. The particle number and XRF intensity is determined for each cycle measurements.

Between 6,000 and 10,000 ADT cycles, the aforementioned 8.3% small particles under 2 nm in size completely disappear, and the size and number of the large particles remains similar respectively at 14.7 ± 5.0 nm (Fig. 3c and Supplementary Fig. 10). This indicates Type I degradation as the dominant pathway between 6,000 and 10,000 ADT cycles. From the discussed observations, we conclude that both types of degradation mechanisms co-exist in the first 6,000 ADT cycles with the Type I/II ratio of 1:1.5 in location L and 1:2.1 for location Q; while Type I mechanism dominates in the additional 4,000 ADT cycles, especially to those small Pt nanoparticles below 2 nm in size.

From a half-cell thin film RDE setup, degradation of electrochemical performance of the Pt/C catalyst is also obtained, in which the mass activity (MA) drops from the initial 0.289 A mg_{Pt}^{-1} to 0.073 A mg_{Pt}^{-1} and 0.048 A mg_{Pt}^{-1}, while the electrochemically active surface area (ECSA) decreases from the initial 70.3 m^2 g_{Pt}^{-1} to 18.2 m^2 g_{Pt}^{-1} and 11.9 m^2 g_{Pt}^{-1} at 6,000 and 10,000 ADT cycles, respectively (Supplementary Fig. 7 and Table 4). The corresponding specific activities remains largely the same at approximately 400 μA cm^{-2}_{Pt}. This is as expected because the intrinsic activity of conventional Pt/C catalyst tend to stay constant, where bulk catalytic activity is loss mainly due to loss of active material and surface area. With the quantified Pt degradation *via* the correlative IL-TEM-XRF technique, the origin of activity loss can be distinguished between type I and II mechanisms. It can be reasoned that the activity degrades in the same proportion as the two types of degradation mechanisms, meaning between both locations, and average of 33.4%, or 0.096 A mg_{Pt}^{-1} of activity degradation can be attributed to type I degradation mechanisms, with 0.120 A mg_{Pt}^{-1} be attributed to type II degradations after 6,000 ADT cycles. Whereas, as established previously, all 0.025 A mg_{Pt}^{-1} of activity loss can be attributed to type I mechanisms in the additional 4,000 ADT cycles (Supplementary Fig. 7a and Table 4).

Quantification of Macro-Scale Pt Redistribution from Carbon Corrosion

To statistically understand the locational dependency of the degradation mechanisms on the catalyst, the 9×9 μm^2 XRF image at each degradation state is segmented into 6 regions based on their relative Pt signal *via* the multi-Otsu thresholding algorithm[46] (Fig. 4a-c, Supplementary

Methods: Imaging Analysis). Cross referencing with the correlative bright field- (BF-)STEM images (Supplementary Fig. 15a-c) reveal that regions classified with the lowest Pt signal, labelled in dark blue, contain mostly carbon film of the TEM grid and are primarily devoid of any catalyst particles and carbon support – these areas are referred as the empty regions. On the other hand, regions classified with intermediate and high Pt signals represent areas with sparser and denser Pt nanoparticle densities (Fig. 4a-c and supplementary Fig. 15d-f). For the pristine catalyst at location L, 47.1% and 29.4% of the total 9.0×9.0 μm^2 area are classified as sparse and dense regions, respectively. After 6,000 ADT cycles, the proportion of the sparse region increase to 59.2% and the dense region decreases to 17.7%, while the area of empty region remains broadly constant (Fig. 4d, Supplementary Fig. 16). These measurements illustrate the redistribution of the Pt/C catalyst, where part of the dense areas disperse into a larger area of the sparser region with a quantified rate of 1.57×10^3 nm^2 per ADT cycle. This quantitation rises to 77% for the measurement in location Q (Supplementary Fig. 17-20). The additional 4,000 ADT cycles further reduce the relative areas of both sparse and dense regions to 54% and 17%, respectively, which represents an overall shrinkage of the Pt/C catalyst into a more heterogeneous distribution, a typical effect of carbon corrosion. As such, the rate of carbon corrosion between 6,000 and 10,000 ADT cycles is quantified to be 1.13×10^3 nm^2 per ADT cycle.

In order to further study the macro-scale Pt redistribution cause by carbon corrosion, an optical flow registration algorithm is applied between the IL-XRF image of the Pt/C catalyst at pristine state and after 6,000 ADT cycles (Fig. 4e and Supplementary Image Analysis). The algorithm generates an optical flow vector field that mimics the Pt signal redistribution between the IL-XRF image pair based on the brightness constancy assumption. Assuming this macro-scale Pt redistribution is mainly induced by carbon corrosion, the magnitude of each flow vector can be interpreted as the range of the catalyst displacement by carbon corrosion at each localised 100×100 nm^2 pixel area and be correlated to the Pt sparse and dense regions (Fig. 4f). As such, the average ranges of catalyst redistribution cause by carbo corrosion are 0.3 ± 0.3 μm, 0.6 ± 0.6 μm, and 1.6 ± 0.9 μm for the Pt empty, sparse, and dense regions, respectively.
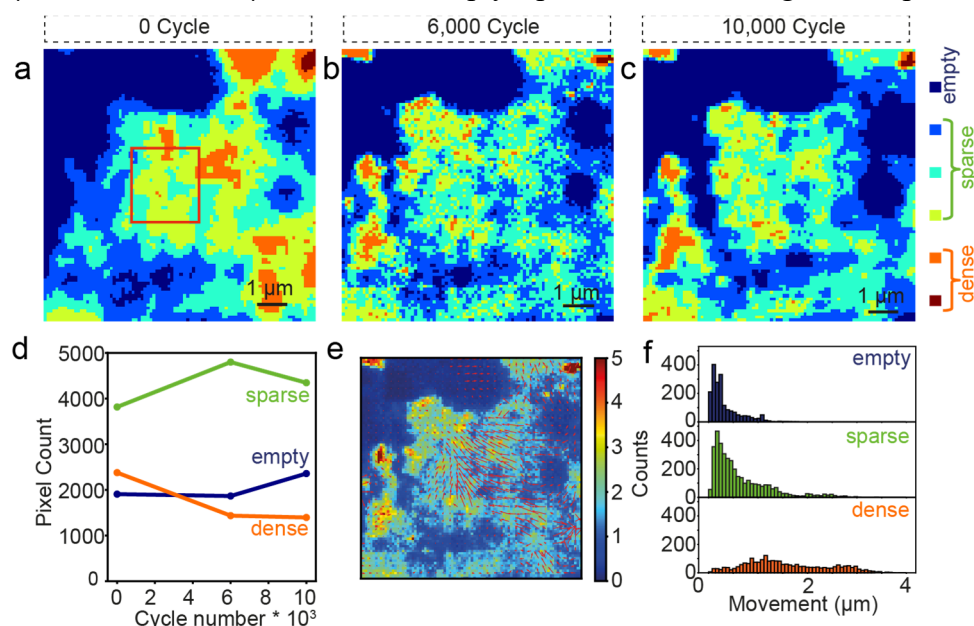

Figure 4. Segmentation of XRF maps after 0, 6,000 and 10,000 ADT cycles at location L. a-c, Segmented XRF map after **a**, 0, **b**, 6,000, and **c**, 10,000 ADT cycles. The colour code from dark blue (segment 1) to dark red (segment 6) indicates regions with the sparsest to the densest Pt nanoparticle distribution. **d**, Variations in pixel counts making up dense, sparse and empty

regions. **e**, Vector field of the simulated Pt redistribution presented as a quiver plot overlayed on the XRF map at 6,000 ADT cycle, the arrows are downscaled for visualisation. **f**, Histogram of the vector magnitudes at different segments from 0 to 6,000 cycles.

Regional statistics of 2D type I and II Degradation Distributions

Both types of degradations can be further quantified into pixel precision resulting in a 2D degradation distributions. First, the obtained vector field (Fig. 4e) is used to computationally warp the XRF image of the degraded catalyst at 6,000 ADT cycles, and that the integrated Pt signal is kept constant (Fig. 5a). Assuming both type I and II degradations are sufficiently short range to have negligible asymmetric macro-scale catalyst redistribution discussed above (Fig. 4), the warped XRF image simulates the degraded catalyst without the influence of carbon corrosion. Second, the pixel-wise application of the same data processing principle for Fig. 3 is performed, deconvoluting type I and II degradation pathways as 2D distributions (Fig. 5b,c) (eq3, Supplementary Image Analysis)

$$Pt_{pristine} = Pt_{Type\ I} + Pt_{Type\ II} + Pt_{remained} \qquad eq3$$

Type II degradation mechanisms are uniformly distributed across the catalyst whereas Type I degradations distribute more significantly towards the centre of the catalyst with high Pt density (Fig. 5b,c). Between the pristine state and 6,000 ADT cycles, the Pt/C catalyst demonstrates a mono-modally distributed type I degradation primarily at regions with less than 500 Pt particle per 100×100 nm^2 area, while that of type II degradation is bimodal distributed at both < 200 and ~1000 Pt particle per 100×100 nm^2 areas (Supplementary Fig. 21). To further investigate this regional dependence of the catalyst degradations, the segmented classifications are applied to both 2D degradation distributions. After 6,000 ADT cycles, 75% of the sparse region is dominated by type II degradations with an average of 787 Pt nanoparticles per 100×100 nm^2 area deactivated, equivalent to a 3.0×10^6 out of the total 4.0×10^6 Pt nanoparticles from the region deactivated through either Ostwald ripening and/or particle agglomeration; whilst the Pt dense region suffers from both Type I and II degradations with 43% and 49% out of the 4.0 $\times 10^6$ nanoparticles within the region, respectively, and an average of 890 and 1029 Pt nanoparticles deactivated per 100×100 nm^2 area. These quantifications can also be expressed in terms of degradation rates of 83.3 and 500 particles per cycle respectively for type I and II mechanisms at the Pt sparse region; and 350 and 400 particles per cycle at the Pt dense region. This also demonstrates that type II degradation dominates in Pt sparse region whereas both types of degradations contribute similarly in Pt dense regions. From 6,000 to 10,000 ADT cycles, type I degradation dominates and occur uniformly on both Pt sparse and dense regions, with respective proportions of 46% and 53% and equivalent particle numbers of 4.7×10^5 and 2.7×10^5, corresponding to 99 and 191 per 100×100 nm^2 area (Fig. 5e).
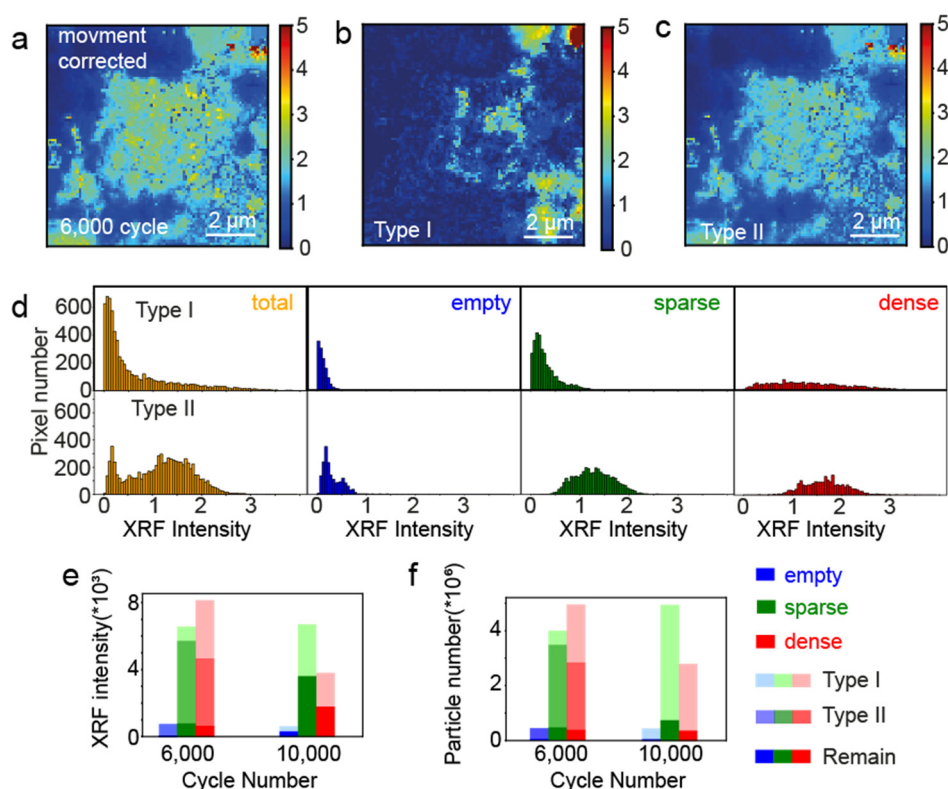
Figure 5. Pixel-wise visualization of the Pt Type I and II degradation. a, Simulated Pt XRF map after 6,000 ADT cycles without the influence of Pt redistribution by carbon corrosion. **b,c** 2D Pt degradation distributions of **b,** type I mechanisms and **c,** type II mechanisms between pristine state and 6,000 ADT cycles. **d,** Pixel count histograms of the degradation distribution at different segments. **e,** XRF intensities and **f,** Pt particle numbers at different segments colour coded to the respective degradation mechanisms.

Conclusion

Correlative IL-TEM-XRF imaging has demonstrated the capability to quantify 2D distributions of Pt content and nanoparticle number of PEMFC Pt/C catalysts in areal size up to $10 \times 10\ \mu m^2$ of the XRF scanned and resolution down to the 100×100 nm^2 of the XRF nanoprobe size. This analysis enables the quantification 2D degradation distributions using the proposed categorisation of Type I and II degradations based on the different effects on the particle size, number, and Pt quantity of the Pt/C catalyst. It is found that in Type I and II contribute to Pt/C catalyst degradation in a ratio of 1:1.5 in the first 6,000 ADT cycles, and type I degradation dominates in the additional 4,000 ADT cycles between 0.4 and 1.2 V *vs.* RHE. Type II degradation tend to be pre-dominant in Pt sparse regions, while both degradation types prevail in Pt dense regions, where Pt is shown to migrate from Pt dense region to Pt sparse region to accommodate for such disproportionate loss in active material. This study has demonstrated the importance of multi-modal, multi-length scale analysis of catalyst material across various stages of activity cycle. The obtained/available quantitative and spatially resolved information is able to bridge between microscopy structure and macroscopic performance in dynamic catalytic systems.

References

1   Ohma, A., Shinohara, K., Iiyama, A., Yoshida, T. & Daimaru, A. Membrane and Catalyst Performance Targets for Automotive Fuel Cells by FCCJ Membrane,

Catalyst, MEA WG. *ECS Transactions* **41**, 775 (2011). https://doi.org/10.1149/1.3635611

2   Zhao, Z. *et al.* Tailoring a Three-Phase Microenvironment for High-Performance Oxygen Reduction Reaction in Proton Exchange Membrane Fuel Cells. *Matter* **3**, 1774-1790 (2020). https://doi.org:https://doi.org/10.1016/j.matt.2020.09.025

3   Dubau, L. *et al.* A review of PEM fuel cell durability: materials degradation, local heterogeneities of aging and possible mitigation strategies. *Wiley Interdiscip. Rev. Energy Environ.* **3**, 540-560 (2014). https://doi.org:10.1002/wene.113

4   Meier, J. C. *et al.* Design criteria for stable Pt/C fuel cell catalysts. *Beilstein Journal of Nanotechnology* **5**, 44-67 (2014). https://doi.org:10.3762/bjnano.5.5

5   Kocha, S. S. in *Polymer Electrolyte Fuel Cell Degradation*   89-214 (Elsevier, 2012).

6   Okonkwo, P. C. *et al.* Platinum degradation mechanisms in proton exchange membrane fuel cell (PEMFC) system: A review. *International Journal of Hydrogen Energy* **46**, 15850-15865 (2021). https://doi.org:https://doi.org/10.1016/j.ijhydene.2021.02.078

7   Nelayah, J. *et al.* Mapping surface plasmons on a single metallic nanoparticle. *Nature Physics* **3**, 348-353 (2007). https://doi.org:10.1038/nphys575

8   Nie, Z., Petukhova, A. & Kumacheva, E. Properties and emerging applications of self-assembled structures made from inorganic nanoparticles. *Nature Nanotechnology* **5**, 15-25 (2010). https://doi.org:10.1038/nnano.2009.453

9   Anker, J. N. *et al.* Biosensing with plasmonic nanosensors. *Nature Materials* **7**, 442-453 (2008). https://doi.org:10.1038/nmat2162

10 Davis, M. E., Chen, Z. & Shin, D. M. Nanoparticle therapeutics: an emerging treatment modality for cancer. *Nature Reviews Drug Discovery* **7**, 771-782 (2008). https://doi.org:10.1038/nrd2614

11 Seipenbusch, M., Toneva, P., Peukert, W. & Weber, A. P. Impact fragmentation of metal nanoparticle agglomerates. *Part. Part. Syst. Charact.* **24**, 193-200 (2007). https://doi.org:10.1002/ppsc.200601089

12 Diwakar, P. K., Loper, K. H., Matiaske, A.-M. & Hahn, D. W. Laser-induced breakdown spectroscopy for analysis of micro and nanoparticles. *J. Anal. At. Spectrom.* **27**, 1110 (2012). https://doi.org:10.1039/c2ja30012e

13 Ray, S., Lalman, J. A. & Biswas, N. Using the Box-Benkhen technique to statistically model phenol photocatalytic degradation by titanium dioxide nanoparticles. *Chem. Eng. J.* **150**, 15-24 (2009). https://doi.org:10.1016/j.cej.2008.11.039

14 Konig, K. Multiphoton microscopy in life sciences. *J. Microsc.* **200**, 83-104 (2000). https://doi.org:10.1046/j.1365-2818.2000.00738.x

15 Bolte, S. & Cordelières, F. P. A guided tour into subcellular colocalization analysis in light microscopy. *J. Microsc.* **224**, 213-232 (2006). https://doi.org:10.1111/j.1365-2818.2006.01706.x

16 Rees, P., Wills, J. W., Brown, M. R., Barnes, C. M. & Summers, H. D. The origin of heterogeneous nanoparticle uptake by cells. *Nat. Commun.* **10**, 2341 (2019). https://doi.org:10.1038/s41467-019-10112-4

17 Summers, H. D. *et al.* Statistical analysis of nanoparticle dosing in a dynamic cellular system. *Nat. Nanotechnol.* **6**, 170-174 (2011). https://doi.org:10.1038/nnano.2010.277

18 Shao-Horn, Y. *et al.* Coarsening of Pt Nanoparticles in Proton Exchange Membrane Fuel Cells upon Potential Cycling. *ECS Transactions* **1**, 185-195 (2006). https://doi.org:10.1149/1.2214553

19 Yu, W. *et al.* Characterising porosity in platinum nanoparticles. *Nanoscale* **11**, 17791-17799 (2019). https://doi.org:10.1039/c9nr06071e

20   Lafforgue, C., Chatenet, M., Dubau, L. & Dekel, D. R. Accelerated Stress Test of Pt/C Nanoparticles in an Interface with an Anion-Exchange Membrane—An Identical-Location Transmission Electron Microscopy Study. *ACS Catalysis* **8**, 1278-1286 (2018). https://doi.org:10.1021/acscatal.7b04055

21   Meier, J. C. *et al.* Degradation Mechanisms of Pt/C Fuel Cell Catalysts under Simulated Start–Stop Conditions. *ACS Catalysis* **2**, 832-843 (2012). https://doi.org:10.1021/cs300024h

22   Dubau, L., Castanheira, L., Berthomé, G. & Maillard, F. An identical-location transmission electron microscopy study on the degradation of Pt/C nanoparticles under oxidizing, reducing and neutral atmosphere. *Electrochimica Acta* **110**, 273-281 (2013). https://doi.org:https://doi.org/10.1016/j.electacta.2013.03.184

23   Hodnik, N. & Cherevko, S. Spot the difference at the nanoscale: identical location electron microscopy in electrocatalysis. *Current Opinion in Electrochemistry* **15**, 73-82 (2019). https://doi.org:https://doi.org/10.1016/j.coelec.2019.03.007

24   Xu, R. *et al.* Improving the ORR performance by enhancing the Pt oxidation resistance. *Journal of Catalysis* **416**, 311-321 (2022). https://doi.org:https://doi.org/10.1016/j.jcat.2022.10.025

25   Leteba, G. M. *et al.* Oleylamine Aging of PtNi Nanoparticles Giving Enhanced Functionality for the Oxygen Reduction Reaction. *Nano Letters* **21**, 3989-3996 (2021). https://doi.org:10.1021/acs.nanolett.1c00706

26   Rasouli, S. *et al.* Electrochemical Degradation of Pt–Ni Nanocatalysts: An Identical Location Aberration-Corrected Scanning Transmission Electron Microscopy Study. *Nano Letters* **19**, 46-53 (2019). https://doi.org:10.1021/acs.nanolett.8b03022

27   Lee, B. *et al.* Statistical characterization of the morphologies of nanoparticles through machine learning based electron microscopy image analysis. *ACS Nano* **14**, 17125-17133 (2020). https://doi.org:10.1021/acsnano.0c06809

28   Muto, S. & Shiga, M. Application of machine learning techniques to electron microscopic/spectroscopic image data analysis. *Microscopy (Oxf.)* **69**, 110-122 (2020). https://doi.org:10.1093/jmicro/dfz036

29   Sorzano, C. O. S. *et al.* Automatic particle selection from electron micrographs using machine learning techniques. *J. Struct. Biol.* **167**, 252-260 (2009). https://doi.org:10.1016/j.jsb.2009.06.011

30   Faraz, K., Grenier, T., Ducottet, C. & Epicier, T. Deep learning detection of nanoparticles and multiple object tracking of their dynamic evolution during in situ ETEM studies. *Sci. Rep.* **12**, 2484 (2022). https://doi.org:10.1038/s41598-022-06308-2

31   Curtis, C. *et al.* Predicting in situ nanoparticle behavior using multiple particle tracking and artificial neural networks. *Nanoscale* **11**, 22515-22530 (2019). https://doi.org:10.1039/c9nr06327g

32   *Correlative imaging*. (Wiley-Blackwell, 2019).

33   Bootz, A., Vogel, V., Schubert, D. & Kreuter, J. Comparison of scanning electron microscopy, dynamic light scattering and analytical ultracentrifugation for the sizing of poly(butyl cyanoacrylate) nanoparticles. *Eur. J. Pharm. Biopharm.* **57**, 369-375 (2004). https://doi.org:10.1016/s0939-6411(03)00193-0

34   Takao, S. *et al.* Mapping platinum species in polymer electrolyte fuel cells by spatially resolved XAFS techniques. *Angew. Chem. Int. Ed Engl.* **53**, 14110-14114 (2014). https://doi.org:10.1002/anie.201408845

35   Takao, S. *et al.* Visualization Analysis of Pt and Co Species in Degraded Pt3Co/C Electrocatalyst Layers of a Polymer Electrolyte Fuel Cell Using a Same-View Nano-

XAFS/STEM-EDS Combination Technique. *ACS Applied Materials & Interfaces* **12**, 2299-2312 (2020). https://doi.org:10.1021/acsami.9b16393

36   Takao, S. *et al.* Observation of Degradation of Pt and Carbon Support in Polymer Electrolyte Fuel Cell Using Combined Nano-X-ray Absorption Fine Structure and Transmission Electron Microscopy Techniques. *ACS Applied Materials & Interfaces* **10**, 27734-27744 (2018). https://doi.org:10.1021/acsami.8b04407

37   Takao, S. *et al.* Same-View Nano-XAFS/STEM-EDS Imagings of Pt Chemical Species in Pt/C Cathode Catalyst Layers of a Polymer Electrolyte Fuel Cell. *The Journal of Physical Chemistry Letters* **6**, 2121-2126 (2015). https://doi.org:10.1021/acs.jpclett.5b00750

38   Mitsushima, S., Koizumi, Y., Uzuka, S. & Ota, K.-I. Dissolution of platinum in acidic media. *Electrochimica Acta* **54**, 455-460 (2008). https://doi.org:https://doi.org/10.1016/j.electacta.2008.07.052

39   Macauley, N. *et al.* Carbon Corrosion in PEM Fuel Cells and the Development of Accelerated Stress Tests. *Journal of The Electrochemical Society* **165**, F3148-F3160 (2018). https://doi.org:10.1149/2.0061806jes

40   Castanheira, L. *et al.* Carbon Corrosion in Proton-Exchange Membrane Fuel Cells: From Model Experiments to Real-Life Operation in Membrane Electrode Assemblies. *ACS Catalysis* **4**, 2258-2267 (2014). https://doi.org:10.1021/cs500449q

41   Shao-Horn, Y. *et al.* Instability of supported platinum nanoparticles in low-temperature fuel cells. *Top. Catal.* **46**, 285-305 (2007). https://doi.org:10.1007/s11244-007-9000-0

42   Mayrhofer, K. J. J. *et al.* Non-destructive transmission electron microscopy study of catalyst degradation under electrochemical treatment. *Journal of Power Sources* **185**, 734-739 (2008). https://doi.org:https://doi.org/10.1016/j.jpowsour.2008.08.003

43   Schlögl, K., Hanzlik, M. & Arenz, M. Comparative IL-TEM Study Concerning the Degradation of Carbon Supported Pt-Based Electrocatalysts. *Journal of The Electrochemical Society* **159**, B677-B682 (2012). https://doi.org:10.1149/2.035206jes

44   Quinn, P. D. *et al.* The Hard X-ray Nanoprobe beamline at Diamond Light Source. *Journal of Synchrotron Radiation* **28**, 1006-1013 (2021). https://doi.org:doi:10.1107/S1600577521002502

45   Quinn, P. D., Gomez-Gonzalez, M., Cacho-Nerin, F. & Parker, J. E. Beam and sample movement compensation for robust spectro-microscopy measurements on a hard X-ray nanoprobe. *Journal of Synchrotron Radiation* **28**, 1528-1534 (2021).

46   Liao, P.-S., Chen, T.-S. & Chung, P.-C. A fast algorithm for multilevel thresholding. *J. Inf. Sci. Eng.* **17**, 713-727 (2001).

Acknowledgement

Author Contributions

# These authors contributed equally to this work.

F.R.W. supervised the study. L.K., R.Xu. and F.R.W. designed the experiments. R.X. preformed the electrochemical cycling. L.K., R.X., F.C.N. and J.P. performed the X-ray nanoprobe measurement. L.K., R.X. and C.S.A performed the HAADF-STEM study. L.K. analyses the XRF and STEM data in Fig. 2 and 3. J.H.C.Y. analysed the XRF data in Fig. 4 and 5. F.R.W. and J.H.C.Y. wrote the manuscript.

Competing interests

The authors declare no competing interests.